Article:
(2024) Measurement of the Se 78 (n,γ) Se 79 cross section up to 600 keV at the n_TOF facility at CERN. Physical Review C. 065805. ISSN: 2469-9993

https://doi.org/10.1103/PhysRevC.110.065805

Measurement of the ^{78}Se(n,γ) ^{79}Se cross section up to 600 keV at the n_TOF facility at CERN

N. V. Sosnin,[1,*] C. Lederer-Woods,[1] R. Garg,[1] U. Battino,[2] S. Cristallo,[3,4] M. Dietz,[1,5] S. Heinitz,[6] M. Krtička,[7] R. Reifarth,[8] S. Valenta,[7] D. Vescovi,[3,4] O. Aberle,[9] V. Alcayne,[10] S. Amaducci,[11,12] J. Andrzejewski,[13] L. Audouin,[14] V. Bécares,[10] V. Babiano-Suarez,[15] M. Bacak,[9,16,17] M. Barbagallo,[9,18] F. Bečvář,[7] G. Bellia,[11,12] E. Berthoumieux,[17] J. Billowes,[19] D. Bosnar,[20] A. Brown,[21] M. Busso,[4,22] M. Caamaño,[23] L. Caballero,[15] F. Calviño,[24] M. Calviani,[9] D. Cano-Ott,[10] A. Casanovas,[24] F. Cerutti,[9] Y. H. Chen,[14] E. Chiaveri,[9,19,25] N. Colonna,[18] G. Cortés,[24] M. A. Cortés-Giraldo,[25] L. Cosentino,[11] L. A. Damone,[18,26] M. Diakaki,[27,9] C. Domingo-Pardo,[15] R. Dressler,[6] E. Dupont,[17] I. Durán,[23] Z. Eleme,[28] B. Fernández-Domínguez,[23] A. Ferrari,[9] P. Finocchiaro,[11] V. Furman,[29] K. Göbel,[8] A. Gawlik-Ramięga,[13] S. Gilardoni,[9] T. Glodariu,[30,†] I. F. Gonçalves,[31] E. González-Romero,[10] C. Guerrero,[25] F. Gunsing,[17] H. Harada,[32] J. Heyse,[33] D. G. Jenkins,[21] E. Jericha,[16] F. Käppeler,[34,†] Y. Kadi,[9] A. Kimura,[32] N. Kivel,[6] M. Kokkoris,[27] Y. Kopatch,[29] D. Kurtulgil,[8] I. Ladarescu,[15] H. Leeb,[16] J. Lerendegui-Marco,[25] S. Lo Meo,[35,36] S. J. Lonsdale,[1] A. Manna,[36,37] T. Martínez,[10] A. Masi,[9] C. Massimi,[36,37] P. Mastinu,[38] M. Mastromarco,[9] F. Matteucci,[39,40] E. A. Maugeri,[6] A. Mazzone,[18,41] E. Mendoza,[10] A. Mengoni,[35] V. Michalopoulou,[27] P. M. Milazzo,[39] A. St. J. Murphy,[1] A. Musumarra,[42,12] A. Negret,[30] R. Nolte,[5] F. Ogállar,[43] A. Oprea,[30] N. Patronis,[28] A. Pavlik,[44] J. Perkowski,[13] L. Piersanti,[18,4,45] I. Porras,[43] J. Praena,[43] J. M. Quesada,[25] D. Radeck,[5] D. Ramos-Doval,[14] T. Rauscher,[46,47] D. Rochman,[6] C. Rubbia,[9] M. Sabaté-Gilarte,[9,25] A. Saxena,[48] P. Schillebeeckx,[33] D. Schumann,[6] A. G. Smith,[19] A. Stamatopoulos,[27] G. Tagliente,[18] J. L. Tain,[15] T. Talip,[6] A. Tarifeño-Saldivia,[24] L. Tassan-Got,[9,27,14] P. Torres-Sánchez,[43] A. Tsinganis,[9] J. Ulrich,[6] S. Urlass,[9,49] G. Vannini,[36,37] V. Variale,[18] P. Vaz,[31] A. Ventura,[36] V. Vlachoudis,[9] R. Vlastou,[27] A. Wallner,[50] P. J. Woods,[1] T. Wright,[19] and P. Žugec[20] (n_TOF Collaboration)[†]

[1]*School of Physics and Astronomy, University of Edinburgh, Edinburgh, United Kingdom*
[2]*E.A. Milne Centre for Astrophysics, Department of Physics and Mathematics, University of Hull, Hull, United Kingdom*
[3]*Istituto Nazionale di Astrofisica - Osservatorio Astronomico d'Abruzzo, Assergi, Italy*
[4]*Istituto Nazionale di Fisica Nucleare, Sezione di Perugia, Perugia, Italy*
[5]*Physikalisch-Technische Bundesanstalt (PTB), Bundesallee 100, 38116 Braunschweig, Germany*
[6]*Paul Scherrer Institut (PSI), Villigen, Switzerland*
[7]*Charles University, Prague, Czech Republic*
[8]*Goethe University Frankfurt, Frankfurt am Main, Germany*
[9]*European Organization for Nuclear Research (CERN), Geneva, Switzerland*
[10]*Centro de Investigaciones Energéticas Medioambientales y Tecnológicas (CIEMAT), Madrid, Spain*
[11]*INFN Laboratori Nazionali del Sud, Catania, Italy*
[12]*Department of Physics and Astronomy, University of Catania, Catania, Italy*
[13]*University of Lodz, Lodz, Poland*
[14]*Institut de Physique Nucléaire, CNRS-IN2P3, Université Paris-Sud, Université Paris-Saclay, F-91406 Orsay Cedex, France*
[15]*Instituto de Física Corpuscular, CSIC - Universidad de Valencia, Valencia, Spain*
[16]*TU Wien, Atominstitut, Stadionallee 2, 1020 Wien, Austria*
[17]*CEA Irfu, Université Paris-Saclay, F-91191 Gif-sur-Yvette, France*
[18]*Istituto Nazionale di Fisica Nucleare, Sezione di Bari, Bari, Italy*
[19]*University of Manchester, Manchester, United Kingdom*
[20]*Department of Physics, Faculty of Science, University of Zagreb, Zagreb, Croatia*
[21]*University of York, York, United Kingdom*
[22]*Dipartimento di Fisica e Geologia, Università di Perugia, Perugia, Italy*
[23]*University of Santiago de Compostela, Santiago de Compostela, Spain*
[24]*Universitat Politècnica de Catalunya, Barcelona, Spain*
[25]*Universidad de Sevilla, Seville, Spain*
[26]*Dipartimento Interateneo di Fisica, Università degli Studi di Bari, Bari, Italy*
[27]*National Technical University of Athens, Athens, Greece*
[28]*University of Ioannina, Ioannina, Greece*
[29]*Affiliated with an institute covered by a cooperation agreement with CERN*

[*]Contact author: nikolay.sosnin@manchester.ac.uk
[†]www.cern.ch/ntof

[30]*Horia Hulubei National Institute of Physics and Nuclear Engineering, Magurele, Romania*
[31]*Instituto Superior Técnico, Lisbon, Portugal*
[32]*Japan Atomic Energy Agency (JAEA), Tokai-Mura, Japan*
[33]*European Commission, Joint Research Centre (JRC), Geel, Belgium*
[34]*Karlsruhe Institute of Technology, Campus North, IKP, 76021 Karlsruhe, Germany*
[35]*Agenzia Nazionale per le Nuove Tecnologie (ENEA), Rome, Italy*
[36]*Istituto Nazionale di Fisica Nucleare, Sezione di Bologna, Bologna, Italy*
[37]*Dipartimento di Fisica e Astronomia, Università di Bologna, Bologna, Italy*
[38]*INFN Laboratori Nazionali di Legnaro, Legnaro, Italy*
[39]*Istituto Nazionale di Fisica Nucleare, Sezione di Trieste, Trieste, Italy*
[40]*Department of Physics, University of Trieste, Trieste, Italy*
[41]*Consiglio Nazionale delle Ricerche, Bari, Italy*
[42]*Istituto Nazionale di Fisica Nucleare, Sezione di Catania, Catania, Italy*
[43]*University of Granada, Granada, Spain*
[44]*University of Vienna, Faculty of Physics, Vienna, Austria*
[45]*Istituto Nazionale di Astrofisica - Osservatorio Astronomico di Teramo, Mosciano Sant'Angelo, Italy*
[46]*Department of Physics, University of Basel, Basel, Switzerland*
[47]*Centre for Astrophysics Research, University of Hertfordshire, Hertfordshire, United Kingdom*
[48]*Bhabha Atomic Research Centre (BARC), Trombay, Mumbai, India*
[49]*Helmholtz-Zentrum Dresden-Rossendorf, Dresden, Germany*
[50]*Australian National University, Canberra, Australia*

(Received 1 July 2024; accepted 18 November 2024; published 17 December 2024)

The ^{78}Se$(n,\gamma)^{79}$Se cross section has a high impact on the abundances of ^{78}Se produced during the slow neutron capture process (*s* process) in massive stars. A measurement of the ^{78}Se radiative neutron capture cross section has been performed at the Neutron Time-of-Flight facility at CERN using a set of liquid scintillation detectors that have been optimized for a low sensitivity to neutrons. We present resonance capture kernels up to 70 keV and cross section from 70 to 600 keV. Maxwellian-averaged cross section (MACS) values were calculated for stellar temperatures between $kT = 5$ and 100 keV, with uncertainties between 4.6% and 5.8%. The new MACS values result in substantial decreases of 20–30% of ^{78}Se abundances produced in the *s* process in massive stars and AGB stars. Massive stars are now predicted to produce subsolar ^{78}Se / ^{76}Se ratios, which is expected since ^{76}Se is an *s*-only isotope, while solar ^{78}Se abundances have also contributions from other nucleosynthesis processes.

DOI: 10.1103/PhysRevC.110.065805

I. INTRODUCTION

Approximately half of the observed elemental abundances in the solar system are attributed to the slow neutron capture process (*s* process), which is defined by a series of neutron captures and β decays starting with an iron seed distribution. The *s* process is characterized by neutron capture rates, which are slower than β-decay rates, causing the process to follow the line of stability closely. The *s*- process is typically subdivided into the weak, main, and strong components, of which the weak *s* process is of particular relevance to this work. This component occurs during He core and C shell burning stages in massive stars with neutron densities of approximately 10^8 cm^{-3} [1], primarily contributing elements between Fe and Sr, which are ejected into the interstellar medium during the later core collapse supernova explosion. The impact of current uncertainties in nuclear reaction rates on predicted abundances in the weak *s* process has been studied by Nishimura *et al.* [2]. They identified that uncertainties in ^{77}Se$(n,\gamma)^{78}$Se and ^{78}Se$(n,\gamma)^{79}$Se have the largest impact on uncertainties of ^{77}Se and ^{78}Se abundances, respectively. The n_TOF Collaboration recently reported a measurement of ^{77}Se$(n,\gamma)^{78}$Se cross section [3], while this work presents the results for the ^{78}Se$(n,\gamma)^{79}$Se reaction.

In stellar environments, particles are in thermal equilibrium and follow a Maxwellian velocity distribution. Hence, the effective interaction cross section is expressed by the Maxwellian-averaged cross section (MACS), which is calculated from the neutron capture cross section averaged over the Maxwellian spectrum. The weak *s* process occurs at stellar temperatures ranging between 0.35 and 1 GK, which corresponds to kT values of $kT \approx 30$ and 90 keV. Currently, the MACS values used in most stellar models come from the KADoNiS v0.3 database [4], which quotes ≈15% cross section uncertainties for all kT values for ^{78}Se.

Cross section measurements used as inputs for MACS calculations should span the neutron energy range of few keV to a few hundred keV. Presently, the nuclear database ENDF/B-VIII.0 [5] relies on data from a compilation by Mughabghab [6], which provides neutron resonance parameters for the ^{78}Se$(n,\gamma)^{79}$Se reaction. The Mughabghab compilation is

TABLE I. Properties of the samples used in the experiment.

Sample	Chemical form	Mass (g)	Diameter (mm)	Sample composition (%)
^{78}Se	metal	1.989	20	^{78}Se(99.39), ^{74}Se(0.04), ^{76}Se(0.04), ^{77}Se(0.17) ^{80}Se(0.32), ^{82}Se(0.04)
^{197}Au	metal	0.5960	20	^{197}Au (100)
C-nat	graphite	2.650	20	^{12}C (98.93), ^{13}C (1.07)

based on several prior measurements [7–9] and provides spin and parity J^π, partial radiative widths Γ_γ, and neutron widths Γ_n for twenty resonances up to 40.5 keV. Further neutron capture cross section data at stellar energies are available on EXFOR [10]. Namely, Kamada *et al.* [11] provide averaged neutron capture cross sections over five energy intervals (four intervals between 15 to 100 keV, and at around ≈550 keV), obtained using the time-of-flight (TOF) technique. Rugel *et al.* [12,13] determined cross sections using a quasi-Maxwellian neutron spectrum around $kT = 25$ keV by activation and subsequent accelerator mass spectrometry (AMS). Two other activation measurements have been performed: one by Herman *et al.* [14] in the 0.5–1.3 MeV neutron energy range, and one by Siddappa *et al.* [15] at 25 keV. In these two measurements, ^{79}Se products were identified using gamma-ray counting.

The details of the experimental campaign presented in this work are provided in Sec. II, data analysis and results are described in Sec. III, the calculation of Maxwellian averaged cross sections and astrophysical implications are discussed in Sec. IV, and a summary is provided in Sec. V.

II. MEASUREMENT

The experiment was performed at the neutron time-of-flight facility n_TOF at CERN [16]. An intense neutron beam was generated by spallation induced in a large lead target using 20 GeV/c proton beams from the Proton Synchrotron (PS). The proton beams are pulsed with a frequency of 0.8 Hz and have an rms time width of 7 ns. Target cooling and neutron moderation are performed using layers of water and borated water around the lead target. The resultant neutron spectrum ranges from thermal (25 meV) to ≈1 GeV. The measurement was performed at the experimental area 1 (EAR-1) flight path at a distance of 185 m from the spallation target, exhibiting an excellent neutron energy resolution (for example, 0.11% at 10 keV neutron energy [16]).

The ^{78}Se sample consisted of 2 g of isotopically enriched (99.39%) Se. The sample was initially in the form of a metal powder, which was subsequently pressed into a cylindrical shape of 2 cm diameter and 1.7 mm thickness. In addition, measurements were performed with a Au sample of the same diameter for normalization, and a natural carbon sample of the same diameter to measure neutron scattering backgrounds. The sample backings were made of a thin Mylar foil stretched on an aluminum holder. Table I provides the details of dimensions, masses, and compositions of the samples used as part of this work.

A capture setup was used for measuring γ rays consisting of four liquid scintillation detectors, filled with deuterated benzene (C_6D_6). The detectors have been specifically optimized to to minimize their sensitivity to scattered neutrons [17]. The detectors were placed 11 cm upstream of the sample position, making an angle of about 125 degrees with respect to the neutron beam. The detector output was digitized using 14-bit analog-to-digital converters (ADCs) at a rate of 1 GHz, which were triggered using a signal from the proton beam just before its arrival at the spallation target. The signals were recorded for 100 ms following the trigger (equivalent to ≈0.02 eV neutron energy), and signal amplitudes and detection times were extracted ofline using a dedicate pulse-shape algorithm [18].

III. DATA ANALYSIS AND RESULTS

A. Experimental capture yield

The neutron flight path was calibrated using well-known low-energy capture resonances in gold [5], and was determined to be 183.95 ± 0.04 m. Then, time-of-flight spectra were converted to neutron energy spectra, and the capture yield $Y(E_n)$ was calculated using the expression

$$Y(E_n) = f(E_n)\frac{C(E_n) - B(E_n)}{\epsilon\Phi(E_n)}. \quad (1)$$

C are measured unweighted counts (pulse height weighting is discussed below) with the sample in-beam at a given neutron energy E_n, B is the background determined as described in Sec. III A 2, ϵ is the capture cascade detection efficiency, Φ is the neutron fluence, and f is a normalization factor, which accounts for the sample not fully covering the neutron beam as well as inaccuracies in detector response simulations (discussed in Sec. III A 3).

1. Detection efficiency

The efficiency of detecting a capture event depends on the specific γ-ray decay path of the compound nucleus. This variation was compensated for by using the total energy detection principle (TED) in conjunction with the pulse height weighting technique (PHWT) [19]. The TED principle can be applied to detection systems with low efficiency, where at most one γ ray per capture event is detected. For a detector where the efficiency of detecting a γ ray, ϵ_γ, is proportional to its energy, E_γ, it can be shown that the efficiency to detect a capture event is proportional to the excitation energy of the compound nucleus, i.e., $\epsilon_c \propto S_n + E_{\rm cm}$ [20,21]. Here, S_n is the neutron separation energy, and $E_{\rm cm}$ is the center-of-mass energy.

γ-ray detectors usually do not exhibit the proportionality of ϵ_γ and E_γ. Proportionality is achieved by applying an amplitude (pulse-height) dependent weight on each detected event. Weighting functions were calculated using simulations

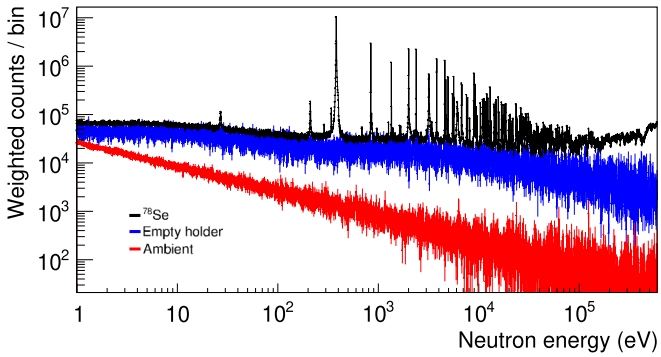

FIG. 1. Weighted counts as a function of neutron energy for the ^{78}Se sample (black), empty sample holder (blue), and ambient experimental area background (red).

of the detector response to monoenergetic γ rays ranging from 200 keV to 10 MeV using the GEANT4 Monte Carlo code [22], based on a detailed geometry of the experimental setup. The analysis threshold for deposited energy $E_{\rm thr} \geqslant 200$ keV was adopted for calculating the weighting functions. To estimate the correction to the yield due to transitions with energies below $E_{\rm thr}$ and transitions without γ-ray emission, cascades were simulated using the code DICEBOX [23,24]. Uncertainties due to the PHWT can be as low as 2% [19]. Considering also the corrections required due to threshold effects, we estimate a 3% uncertainty on the capture yield from the application of PHWT.

2. *Background subtraction*

Background events in our spectra stem from ambient background present in the experimental area without the beam, in-beam background from neutron reactions not originating from the sample (measured with beam and an empty target holder), and elastic neutron scattering background from the sample. Figure 1 shows spectra of the ambient and in-beam backgrounds compared to the ^{78}Se sample. While the ambient background is important at low neutron energies, the in-beam background (empty holder) contributes over the whole neutron energy range of interest.

The scattering component of the background originates from neutrons scattered in the sample and being captured in the surrounding material and producing γ rays. In the resolved resonance region (RRR), a constant background was assumed over the width of a resonance. For the unresolved resonance region (URR) above 70 keV neutron energy, a natural carbon sample (see Table I) was used to estimate the level of this background component. The neutron scattering to capture cross section ratio in natural carbon is $\approx 2 \times 10^5$ in the relevant energy region [25]. The yield measured with the carbon sample was scaled by sample areal densities and scattering cross sections of carbon and ^{78}Se, respectively, and then subtracted from the ^{78}Se spectrum. The level of this background relative to ^{78}Se capture was around 15% on average. 10% uncertainty in the background determination was assumed, originating mainly from uncertainties in the ^{78}Se scattering cross section based on TENDL 2021 evaluation [26], resulting in an uncertainty on the capture yield due to the background subtraction of 1.5%.

3. *Neutron fluence and normalization*

The neutron flux as a function of neutron energy at n_TOF EAR-1 was evaluated using the reference reactions ^{10}B(n,α) and ^{235}U(n,f) [27], with uncertainties ranging from 1% to 5% in the energy range of interest. A further check of neutron fluence is provided by off-beam silicon detectors using ^{6}Li(n,t) reactions on a thin ^{6}LiF sample deposited on a Mylar backing.

The normalization f was determined using the gold resonance at 4.9 eV in conjunction with the saturated resonance technique [28]. The size of the neutron beam, and hence the normalization, varies slightly with neutron energy, requiring corrections to the capture yield of at most 2%. This correction was determined in neutron transport simulations from the lead target to the experimental area and confirmed with dedicated measurements [16]. The resulting uncertainty of $f(E_n)$ is 1%.

B. Parameters of isolated resonances

The multilevel, multichannel R-matrix code SAMMY [29] was used for analysis of the resonances observed in the capture yield spectra. SAMMY fits are used to extract resonance parameters: resonance energy E_R, and neutron and radiative widths Γ_n and Γ_γ, for a given resonance spin J and parity π. Resonance broadening due to thermal motion of atoms (Doppler broadening) and the resolution of the experimental facility are taken into consideration during the fitting. SAMMY also accounts for the effects of multiple interaction and self-shielding of neutrons in the sample. Typically, capture experiments cannot be used alone to determine all resonance parameters of interest for a given resonance (Γ_γ, Γ_n, E_R, J, and π), but in addition to E_R the resonance fits are also sensitive to the resonance capture kernels K defined as

$$K = g\frac{\Gamma_\gamma \Gamma_n}{\Gamma_\gamma + \Gamma_n}, \tag{2}$$

with

$$g = \frac{2J+1}{(2I+1)(2s+1)}, \tag{3}$$

where $I = 0$ is the spin of the ground-state of the target nucleus ^{78}Se, and $s = \frac{1}{2}$ is the neutron spin. The extracted resonance energies and kernels up to 70 keV along with fitting uncertainties are listed in Appendix A. A bound level representing an s-wave resonance was taken into account for the SAMMY cross section calculation, with an energy of -3.870 keV, a gamma width of 236 meV, and a neutron width of 4216 meV based on Ref. [30].

Systematic uncertainties in the RRR comprise 3% from PHWT, 1% from normalization, 1% to 5% from flux, and a 0.01% in sample composition and mass, yielding a total systematic uncertainty of 3.3% below neutron energy of 100 eV, 3.7% between 100 eV and 10 keV, and 5.9% above 10 keV. Examples of SAMMY fits for several neutron energy regions are shown in Fig. 2.

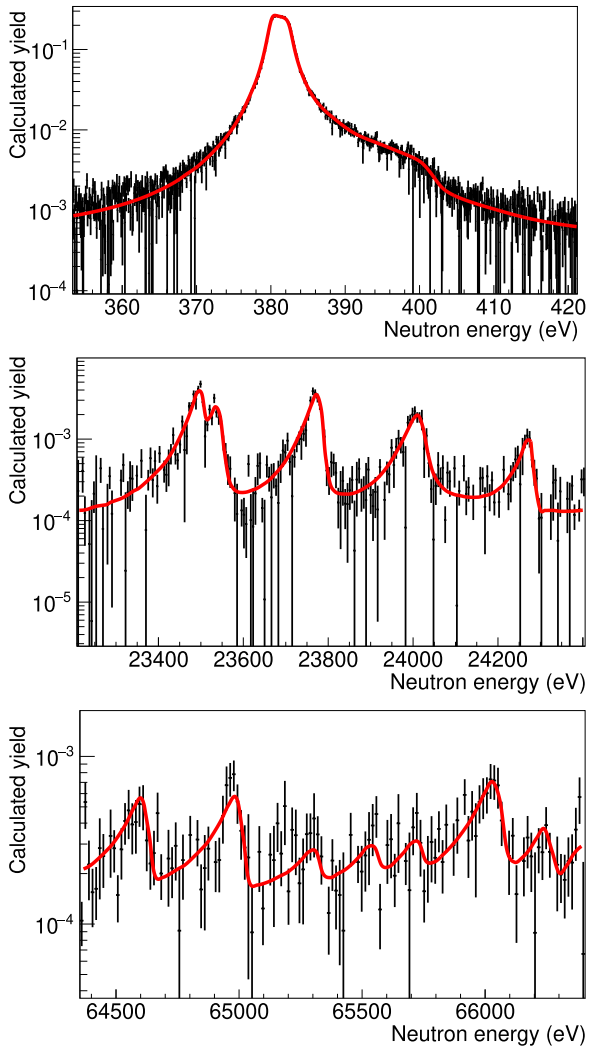

FIG. 2. Examples of SAMMY fits (red) to ^{78}Se$(n,\gamma)^{79}$Se yield data (black) for several neutron-energy regions.

C. Unresolved resonance region

Individual resonance structures are considered in the analysis up to 70 keV, while data between 70 and 600 keV are treated as the URR. The upper limit was chosen to avoid the background from inelastic neutron scattering due to the presence of an excited state at 614 keV in ^{78}Se [31]. As mentioned in Sec. III A 2, the carbon sample was used to subtract the neutron scattering background, which contributed 1.5% to the URR-specific uncertainty along with the systematic uncertainty contributions listed in Sec. III B. Multiple neutron interactions and self-shielding effects were investigated using a Monte Carlo code, which takes into account the sample properties as well as neutron capture and scattering cross sections from the ENDF/B-VIII.0 library [5]; however, the resulting correction was found to be negligible. The flux uncertainty is 5% up to 100 keV neutron energy and 2% in the 100–600 keV energy region. The total systematic uncertainty in URR is thus 6.2% below and 4.2% above 100 keV.

At higher E_n, especially those close to the adopted URR limit, capture events may also occur in which the formed ^{79}Se nucleus is at an excitation energy higher than the neutron separation energy (6962.83 keV [32]) even after γ-ray emission and may subsequently decay via neutron emission. Using DICEBOX code, we verified that the fraction of such events is very small, below 10^{-3} for $E_n = 600$ keV, and therefore this effect has been neglected in the analysis.

TABLE II. Cross sections for several average neutron energies measured by Kamada *et al.* [11] compared to results obtained in our work. Uncertainties in our data represent both the statistical and systematic contributions.

Average energy (range) (keV)	Cross section (mb) Kamada *et al.*	Cross section (mb) n_TOF
20 (15–25)	89.5 ± 4.3	89.8 ± 6.8
30 (25–35)	86.6 ± 3.7	90.8 ± 6.3
44 (35–55)	67.5 ± 2.9	76.4 ± 5.2
69 (55–100)	54.1 ± 2.2	49.8 ± 3.2
550 (460–622)	31.4 ± 1.4	38.0 ± 1.7

D. Comparison with available cross section data

Our URR cross section can be compared with time-of-flight data obtained by Kamada *et al.* [11]. Kamada *et al.* provide spectrum averaged cross sections in four energy intervals from 15 to 100 keV, and also at ≈550 keV, where the neutron energy distribution has a spread of a few tens of keV, as shown in Fig. 2 of Ref. [11]. For comparison, we average our cross sections over the same neutron energy spectrum as the data by Kamada *et al.* [33]. This comparison is shown in Table II.

Our averaged cross sections are in good agreement for the 15–25 and 25–35 keV neutron energy intervals, while our value for the 35–55 keV region is 13% higher (1.5 standard deviations), and 8% lower for the 55–100 keV region (1.1 standard deviations). Our value for the ≈550 keV range is 21% higher (3 standard deviations).

There are three activation measurements we can further compare our results to. The measurement performed by Siddappa *et al.* [15] used a Sb-Be neutron source producing 25 ± 5 keV neutrons. The reported 98 ± 14 mb cross section in that measurement is in agreement within uncertainties with our value of 92.8 ± 5.8 mb averaged over 20–30 keV neutron energy range. The only remaining measurement provided on EXFOR [10] is an activation measurement by Herman *et al.* [14] using neutrons from the ^{3}H$(p,n)^{3}$He reaction. Of the four neutron energy bins investigated therein, only the 530(140)-keV bin partly overlaps with our measurement. If our data are supplemented by normalized JENDL-5 [34] data above 600 keV (discussed in Sec. IV), our averaged cross section from 390–670 keV is 36.2 ± 2.3 mb, which is considerably larger than than the 15.6 ± 2.6 mb value reported by Herman *et al.* The 25-keV cross section obtained by Rugel *et al.* [12] is addressed in Sec. IV below due to the approximately Maxwellian nature of the neutron flux used in that measurement, allowing for comparison between our MACS and their work.

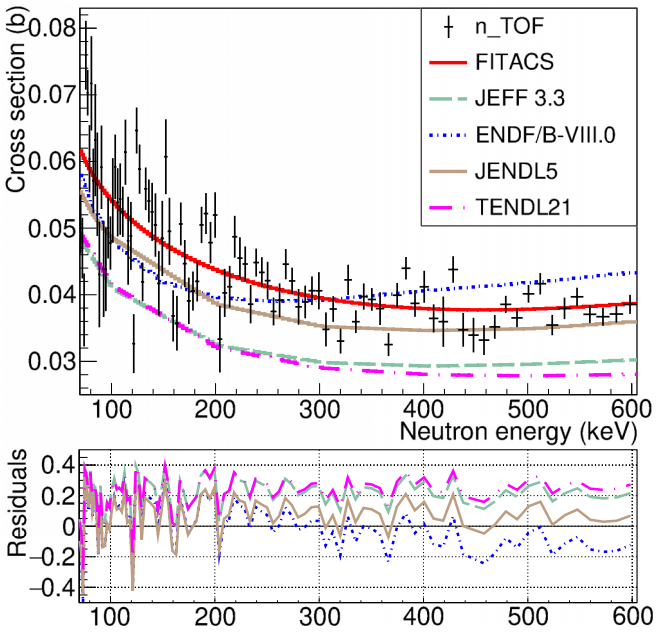

FIG. 3. ^{78}Se$(n,\gamma)^{79}$Se cross sections from 70 to 600 keV and FITACS [35] fit to our data. Our results are shown alongside evaluations [5,25,26,34], and residuals are shown in the bottom panel. The residuals here are defined as the difference between our data and evaluation divided by our data.

Figure 3 shows our URR cross section compared to recent evaluations ENDF/B-VIII.0 [5], JEFF 3.3 [25], JENDL-5 [34], and TENDL 2021 [26]. JEFF and TENDL underestimate our cross section by around 20%; JENDL is consistently lower by around 7%; and ENDF agreement varies substantially across different neutron energy intervals, from underestimating our data by ≈10% between 100 and 200 keV, to near-perfect agreement in the 200–400 keV region, to overestimating the data by ≈11% in the 500–600 keV region.

E. Average resonance parameters

Analysis of individual resonance parameters obtained from SAMMY fits was performed with the aim of constraining average resonance parameters. Although we list only resonance energies and kernels K in Table V (Appendix A), additional information can be reliably obtained in some cases. Specifically, for resonances with $\Gamma_n \gg \Gamma_\gamma$ (and Γ_n not significantly smaller than experimental energy resolution), both $g\Gamma_\gamma$ and Γ_n can be reasonably determined. Resonances at low E_n with large Γ_n are then definitely of s-wave ($\ell = 0$) nature. These resonances of spin $J = \frac{1}{2}$ ($g = 1$) along with their Γ_γ and Γ_n values are listed in Table VI (Appendix B). We verified that there is only a very low probability (exact value of which depends on actual value of neutron strength function for $\ell = 1$ neutrons, S_1) that any of these resonances is of p-wave origin.

In practice, as indicated by Fig. 2, the resolution of individual resonances might become difficult at larger neutron energies, and some of the fitted structures above neutron energies of about 30–40 keV could correspond to resonance multiplets. We thus considered only resonances below 30 keV in the determination of average resonance parameters.

To estimate $\langle\Gamma_\gamma^{\ell=0}\rangle$, we exploited resonances listed in Table VI. For all but the resonance at 382 eV, SAMMY fits yield $\Gamma_n > 20$ K; in these cases, the capture kernel K is practically determined by $g\Gamma_\gamma$. The parameters of the 382 eV resonance are then also deemed reliable based on observations in Refs. [7–9]. These resonances yield $\langle\Gamma_\gamma^{\ell=0}\rangle = 203(11)$ meV. The relative width of Γ_γ distribution is expected to reach 10–30% according to statistical-model calculations performed with the DICEBOX code [23,24], while the experimental value is close to 30%. The $\langle\Gamma_\gamma^{\ell=0}\rangle$ value is in a perfect agreement with the RIPL-3 [36] value of 230(60) meV, but deviates by more than one standard deviation from 173(18) meV in the latest issue of the Atlas of Neutron Resonances [30]. We would like to note that the value in Ref. [30] is based on the analysis of the cross section in the unresolved resonance region and it is not consistent with any isolated resonance results published in the past [7–9].

Strong resonances in Γ_n can be also used to determine the s-wave neutron strength S_0. From the sum of reduced neutron widths, $\Gamma_n\sqrt{1\text{ eV}/E_n}$, we obtained $S_0 = 1.6(4) \times 10^{-4}$; this result is consistent for all available neutron energies. References [30] and [36] evaluate $S_0 = 1.28(49) \times 10^{-4}$ and $1.30(40) \times 10^{-4}$, respectively, in a good agreement with our value.

Similarly to several previous n_TOF measurements [3,37,38], average s-wave level spacing D_0 was determined by counting resonances with kernels above a threshold as predicted by statistical model simulations. As p-wave resonances significantly contribute, the spin and parity dependence or level density must be considered. The spin dependence for the back-shifted Fermi-gas model from Ref. [39] was assumed along with parity independence. Following tests with several thresholds and maximum neutron energies, the resulting D_0 was found to be 1400(150) eV. We checked that different assumptions on spin dependence yield fully consistent D_0. References [30] and [36] provide $D_0 = 1480(200)$ and 1500(300) eV, again in a very good agreement with our result.

Values of average resonance quantities for $\ell = 1$ available in literature typically suffer from very large uncertainty: Ref. [30] evaluates $S_1 = 1.73(100) \times 10^{-4}$ and $D_1 = 515(350)$ eV, while Ref. [36] $S_1 = 3.5(10) \times 10^{-4}$ and $D_1 = 500(250)$ eV. The only quantity with a small uncertainty is $\langle\Gamma_\gamma^{\ell=1}\rangle = 172.8(8.7)$ meV from [30] but this quantity is (similarly to $\langle\Gamma_\gamma^{\ell=0}\rangle$) derived from a fit to the cross section data.

Although determination of $\langle\Gamma_\gamma^{\ell}\rangle$ for $\ell > 0$ from only capture data is rather complicated, SAMMY fits indicate that $\langle\Gamma_\gamma^{\ell=1}\rangle$ is close to $\langle\Gamma_\gamma^{\ell=0}\rangle$. Similar values of $\langle\Gamma_\gamma\rangle$ for resonances of all involved spins and parities are indeed expected from statistical model calculations with DICEBOX code [23,24]; the possible difference of $\langle\Gamma_\gamma\rangle$ depends on models of level density and γ-ray strength functions used and is typically about 10%, although it can reach up to about 20%.

Assuming the above-determined value of S_0 (needed for estimates of contribution of s-wave resonances) and the channel radius $R = 1.23A^{1/3} + 0.8$ fm $= 6.06$ fm [40], we also tried to estimate the p-wave neutron strength S_1. Data for all

TABLE III. Neutron strengths S_ℓ and average radiative widths $\langle\Gamma_\gamma^\ell\rangle$ obtained from FITACS fits for different values of s-wave resonance spacing D_0 and $\ell_{\max}$, the maximum considered ℓ contribution. Note that FITACS assumes $\langle\Gamma_\gamma^{\ell=0}\rangle = \langle\Gamma_\gamma^{\ell=2}\rangle$ and $\langle\Gamma_\gamma^{\ell=1}\rangle = \langle\Gamma_\gamma^{\ell=3}\rangle$. For comparison, values obtained from RRR are shown in the last line.

D_0 (eV)	$\ell_{\max}$	S_0 ($\times10^{-4}$)	S_1 ($\times10^{-4}$)	S_2 ($\times10^{-4}$)	S_3 ($\times10^{-4}$)	$\langle\Gamma_\gamma^{\ell=0}\rangle$ (meV)	$\langle\Gamma_\gamma^{\ell=1}\rangle$ (meV)
1400	2	1.88(50)	2.84(68)	1.42(24)		248(9)	213(15)
1400	3	1.88(50)	2.86(69)	1.89(37)	0.40(12)	209(12)	209(15)
1500	2	1.89(50)	2.91(70)	1.56(25)		265(9)	220(16)
1500	3	1.89(50)	2.91(71)	2.15(42)	0.46(13)	220(12)	214(16)
1400(150)		1.6(4)	2.9(8)			203(11)	

neutron energies are then consistent with $S_1 = 2.9(8) \times 10^{-4}$. Finally, our aforementioned result for D_0 means that $D_1 =$ 490(50) eV from our data.

We also estimated average resonance parameters using our cross section in the URR (i.e., for energies 70–600 keV) with the help of the FITACS package [29,35], which uses Hauser-Feshbach theory to calculate cross section based on user-provided partial radiative widths Γ_γ^ℓ and neutron strength functions S_ℓ for an adjustable range of neutron orbital momenta ℓ, as well as s-wave level spacing D_0. To get a reasonable fit, we had to consider maximum neutron orbital momentum of at least $\ell_{\max} = 2$. In practice, predictions of TALYS code [41] indicate that $\ell_{\max} = 3$ should be used.

Resonance parameters obtained for two different assumed values of D_0 and $\ell_{\max}$ are listed in Table III (the fit shown in Fig. 3 corresponds to $D_0 = 1400$ eV and $\ell_{\max} = 3$; however, fits for all the settings shown in Table III are visually indistinguishable). Channel radius was set to 6.06 fm. Fixing D_0 to 1400 eV yields $D_1 = 487$ eV, $D_2 = 317$ eV, and $D_3 =$ 257 eV, while fixing D_0 to 1500 eV results in $D_1 = 521$ eV, $D_2 = 340$ eV, and $D_3 = 275$ eV. These average resonance parameters for $\ell_{\max} = 3$ are in a good agreement with those extracted from resolved resonances for $\ell = 0$ and $\ell = 1$. We have a few comments about the FITACS results. First, use of slightly different D_0 yields virtually unchanged S_ℓ, while $\langle\Gamma_\gamma\rangle$ is modified in the way that $\langle\Gamma_\gamma\rangle/D$ remains the same. Second, the cross section is dominated by $\ell = 1$ contribution from a few keV up to about 150 keV and by $\ell = 2$ up to the maximum considered energy of 600 keV. Finally, we would like to stress that the actual cross section in individual presented bins is expected to fluctuate around a smooth trend given by FITACS due to contribution of finite number of resonances. The observed fluctuations are fully consistent with the expectation from statistical model predictions.

IV. STELLAR CROSS SECTIONS AND ASTROPHYSICAL IMPLICATIONS

The Maxwellian averaged cross section (MACS) is defined as

$$\text{MACS} = \frac{2}{\sqrt{\pi}}\frac{1}{(kT)^2}\int_0^\infty E\sigma(E)\exp\left(-\frac{E}{kT}\right)dE. \quad (4)$$

In this work, the MACS was calculated based on a cross section comprising three neutron-energy regions: (i) RRR based on SAMMY results below 70 keV, (ii) URR based on our data between 70 and 600 keV, and (iii) normalized evaluated cross section from 600 keV to 10 MeV based on JENDL-5 [34]. Since the JENDL-5 cross section was consistently lower by 7% compared to our data in the overlapping energy region, we scaled the evaluation by a factor of 1.07 (see Fig. 3). The evaluation component of the cross section contributes a small fraction of the final MACS, providing around 1% of the MACS value for $kT = 100$ keV. There is no uncertainty in the JENDL-5 evaluation of ^{78}Se, but for that isotope both JENDL-5 and TENDL are based on state-of-the-art models and parameters that can produce cross section with similar uncertainties, which are available in TENDL. Based on the version TENDL-2019 [26], an uncertainty of 60% was assigned to the evaluation component.

MACSs were calculated for values of kT between 5 and 100 keV, and the results of the calculation along with the uncertainties are listed in Table IV. Furthermore, the table lists MACS values from the KADoNiS v0.3 database [4], which are based on the measurement in Ref. [13] analyzed with AMS and based on a quasi-Maxwellian neutron spectrum for $kT = 25$ keV (and which presents preliminary results of the measurement discussed in full by Rugel *et al.* [12]). MACS uncertainties obtained in this work range from 4.6% to 5.8%, and MACS values are ≈50% larger than KADoNiS for all kT.

The TENDL 2021 library [26] lists MACS predictions for $kT = 30$ keV obtained with different model sets implemented in the TALYS 1.96 reaction code [41]. Considering 12 "preferred" models, the predicted MACS values range from

TABLE IV. Maxwellian-averaged cross section values calculated for the ^{78}Se(n,γ) reaction presented in this work compared to evaluated MACS available in KADoNiS v0.3 for energies kT between 5 and 100 keV.

kT (keV)	n_TOF MACS (mb)	KADoNiS v0.3 MACS (mb)
5	247 ± 11	160
10	165.4 ± 8.6	109
15	130.4 ± 7.2	87
20	111.7 ± 6.3	74
25	98.1 ± 5.7	66
30	89.5 ± 5.2	60±10
40	78.4 ± 4.4	52
50	71.5 ± 3.9	46
60	67.8 ± 3.6	43
80	60.5 ± 3.1	38
100	56.3 ± 2.8	35

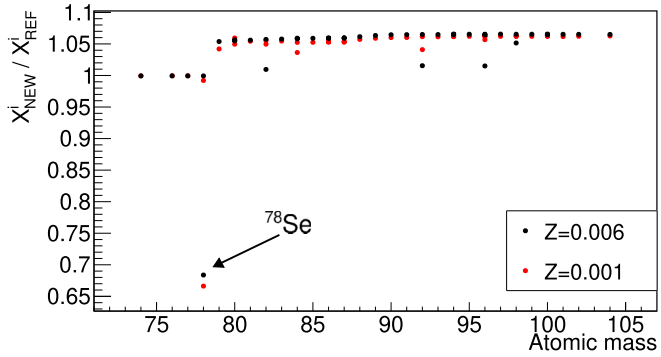

FIG. 4. Impact on $15M_\odot$ stellar abundances for $Z = 0.006$ (in black) and $Z = 0.001$ (in red) based on $^{78}\mathrm{Se}(n,\gamma)^{79}\mathrm{Se}$ MACS calculated in this work. The Y axis shows ratio of abundances X^i_{NEW} calculated as part of this work divided by abundances X^i_{REF} based on KADoNiS v0.3.

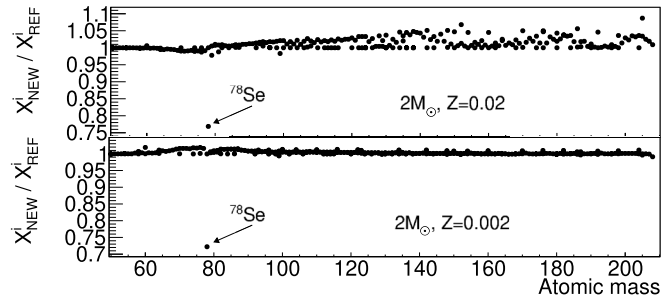

FIG. 5. Impact on $2M_\odot$ stellar abundances for $Z = 0.02$ (top panel) and $Z = 0.002$ (bottom panel) based on $^{78}\mathrm{Se}(n,\gamma)^{79}\mathrm{Se}$ MACS calculated in this work. Vertical axis shows ratio of abundances X^i_{NEW} calculated based on this work divided by abundances X^i_{REF} based on KADoNiS v0.3.

69.0 to 81.0 mb, with ten values in the range of 78–81 meV. Our experimental value, 89.5 ± 5.2 mb, disagrees with all of these 12 models.

The impact of the new MACS values on stellar nucleosynthesis was studied for two massive star models and one low-mass AGB star model at different metallicities. The massive star structures are both from Ref. [42], with an initial mass of $15M_\odot$ and initial subsolar metallicities $Z = 0.006$ and $Z = 0.001$. The full nucleosynthesis was calculated by performing a postprocessing step, using the multizone nucleosynthesis code MPPNP [43]. The abundances were extracted at the end of carbon shell burning. The impact of our new MACS values on stellar abundances is shown in Fig. 4, comparing MPPNP runs using the standard nuclear reaction network (including the new ^{77}Se MACS from Ref. [3]), and with the new ^{78}Se MACS obtained in this study. The ^{78}Se abundance was reduced by about 30%, while there are also small effects on abundances of heavier isotopes.

Furthermore, the ratio of abundances of ^{78}Se to the *s*-only isotope ^{76}Se was found to be approximately 1.8 for $Z = 0.006$ and 2.2 for $Z = 0.001$. This difference is due to a higher activation of the $^{22}\mathrm{Ne}(\alpha,n)^{25}\mathrm{Mg}$ neutron source in the hotter and denser $Z = 0.001$ model. This leads to a higher neutron density and, considering how the typical peak neutron density during carbon-shell burning is a few times 10^{12} cm^{-3} [42], to a higher rate of neutron capture on the unstable ^{76}As (half-life of 26.254 hours [44]), hence "bypassing" ^{76}Se. Our new MACS allow for the calculated ratio of abundances at both metallicities to be below the solar value of 2.5, unlike using default KADoNiS values, which results in a ratio of ≈2.6. This represents a remarkable improvement in the comparison with observations. Indeed, ^{78}Se is expected to be produced also by the *r* process, hence, its abundance ratio to the *s*-only ^{76}Se at the end of carbon shell burning must be below the observed solar ratio.

Although AGB stars do not provide the dominant contribution to the galactic selenium budget (for example, see Fig. 11 of Prantzos *et al.* [45]), we calculated $2M_\odot$ AGB models using the FUNS code [46–48] with metallicities representative of the galactic halo ($Z = 0.002$) and disk ($Z = 0.02$). The adoption of the new MACS lowered the predicted surface abundance of ^{78}Se at the end of the AGB phase by 28% and 23%, respectively. By contrast, only minor variations are found for other heavy element isotopes. Full results are shown in Fig. 5.

V. SUMMARY

A measurement of the $^{78}\mathrm{Se}(n,\gamma)^{79}\mathrm{Se}$ cross section up to neutron energy of 600 keV was performed at the n_TOF facility, CERN. Energies and kernels of more than 200 resonance structures up to 70 keV neutron energy were extracted using the R-Matrix code SAMMY, significantly expanding the list of 20 previously-identified resonances reported in the available nuclear data libraries. As individual resonances cannot be reasonably identified above 70 keV, we determined only the cross section above that energy. The upper reached limit, 600 keV, is given by the opening of inelastic scattering channel slightly above this energy. FITACS code was used to fit the obtained 70–600 keV cross section, and the extracted average resonance parameters were found to be in agreement with the results derived from individual resonances fitted with SAMMY.

The measured cross section was used in combination with data from JENDL-5 to calculate MACS for kT values between 5 and 100 keV, which were found to be ≈50% larger for all kT than those evaluated in the KADoNiS v0.3 database. The impact of the obtained MACS values on calculated *s*-process ^{78}Se abundances was investigated for four stellar models. 32% reduction in abundances was identified for $15M_\odot$, $Z = 0.006$ stellar model, and 28% and 23% decreases were found for $2M_\odot$ stellar models with respective metallicities of $Z = 0.002$ and $Z = 0.02$.

ACKNOWLEDGMENTS

This work was supported by the UK Science and Facilities Council (ST/M006085/1), the European Research Council ERC-2015-StG No. 677497, the MSMT of the Czech Republic, the Charles University UNCE/24/SCI/016 project, National Science Centre, Poland (Grant No. UMO-2021/41/B/ST2/00326), Croatian Science Foundation project IP-2022-10-3878, and by the funding agencies of the participating institutes.

APPENDIX A: RESONANCE ENERGIES AND KERNELS

See Table V for a list of ^{78}Se capture resonance energies and kernels extracted using SAMMY as part of this work.

TABLE V. Resonance energies and kernels identified in ^{78}Se$(n,\gamma)^{79}$Se reaction. Listed uncertainties represent only the fitting contribution, and systematic uncertainties are discussed in text. Bound level information based on Ref. [30] used for RRR cross section calculation was of *s*-wave character and had energy of -3.870 keV, $\Gamma_\gamma = 236$ meV, and $\Gamma_n = 4216$ meV.

Energy (eV)	Kernel (meV)
381.862(4)	102.8(2)
843.951(8)	14.7(1)
1350.99(2)	14.1(2)
1627.1(1)	0.59(6)
2012.05(3)	164(1)
2389.11(2)	87(1)
3198.7(2)	204(3)
3822.67(3)	202(5)
4599.17(4)	171(3)
4716.66(7)	66(2)
4950.97(7)	82.2(1)
5484.1(1)	39(1)
5635.2(1)	155(3)
5684.3(2)	30(1)
6123(1)	215(7)
6259.1(3)	12(1)
6730.95(9)	113.13(3)
6791.8(2)	186(5)
7567.4(1)	81(2)
7762.7(2)	70(3)
8146.3(2)	25(1)
8965.0(9)	26(5)
8976.5(7)	41(8)
8994.3(2)	382(11)
9200.1(3)	119(13)
9217(2)	141(19)
9436.3(2)	79.8(1)
9664.2(4)	39(3)
10378.8(2)	80(4)
10908(3)	287(20)
10980.2(3)	181(11)
11302.9(2)	144(6)
11628.0(3)	125(6)
12053.7(2)	196(8)
12360.0(4)	219(8)
12979.0(3)	400(12)
13296.9(3)	47(39)
14214.3(3)	147(7)
14280.4(6)	72(5)
14467.9(3)	156(16)
14783.7(3)	252(13)
14947.8(3)	208(2)
15658.5(4)	282(14)
15877.6(4)	120(6)
16839.2(4)	282(16)
17032.3(6)	258(13)
17135.3(5)	148(8)
17854.9(4)	318(15)
18035.4(6)	133(9)
18359.9(8)	63(19)
18595.8(5)	267(19)
18672(3)	244(17)
19804.9(9)	55(29)
19978(2)	157(11)
20258.2(7)	125(8)
20320(1)	126(9)
20629.3(9)	152(12)
20812(2)	47(7)
20908.8(8)	119(8)
21142.9(2)	109(85)
21901(2)	230(17)
23534.1(8)	184(106)
23577(1)	217(19)
23813.8(8)	286(17)
24054(2)	214(14)
24311.0(4)	62(45)
24931.0(2)	88(72)
25634.3(4)	260(53)
25958(2)	229(15)
26226(2)	148(52)
26274(2)	135(16)
26321.4(2)	96(79)
26367(3)	49(13)
26613.7(2)	131(97)
26867.5(9)	346(20)
27507(3)	237(21)
27853(1)	247(15)
28090(1)	148(47)
28322(1)	441(24)
29159(7)	140(23)
29288(3)	220(27)
29392(2)	351(27)
29645.8(8)	98(65)
29865(2)	351(21)
30747(1)	312(22)
31090(1)	405(28)
31368(1)	240(17)
31461.3(7)	134(95)
31860(12)	303(47)
31931(2)	246(28)
32549.7(4)	301(203)
32863(2)	156(15)
33306(2)	442(34)
34337.5(2)	64(49)
34531.1(2)	112(90)
34604.1(5)	143(104)
34779.8(3)	42(35)
34962.7(2)	83(67)
35015.1(3)	144(108)
35306(4)	521(47)
35656(2)	352(72)
35801.9(6)	122(84)
35960.6(2)	51(37)
36150.3(4)	52(44)

TABLE V. *(Continued.)*

Energy (eV)	Kernel (meV)
36534(2)	208(24)
37444.9(2)	65(58)
37621(3)	279(39)
37701(2)	276(37)
37913.8(5)	90(76)
38110(5)	198(31)
38251(3)	272(65)
38710(6)	185(27)
39083(7)	206(32)
39302(4)	368(38)
39492.6(3)	107(87)
39875(6)	228(33)
40495.0(5)	168(120)
41149.7(3)	98(80)
41218(5)	374(47)
41829(3)	266(27)
42161(4)	397(35)
42405(3)	300(30)
42736(4)	507(38)
43254.8(2)	43(39)
43593(4)	262(38)
43835.8(2)	169(127)
43938.7(8)	100(79)
44040(14)	756(91)
44628(3)	343(33)
45239(4)	460(37)
45444(4)	197(28)
45893.7(3)	218(153)
45980(3)	487(51)
46482(4)	433(38)
47126.0(2)	114(90)
47661(5)	609(47)
48031(3)	328(31)
48276(4)	270(35)
48576(4)	177(26)
49026(5)	230(30)
49251(9)	241(36)
49647(3)	329(41)
49907(7)	180(32)
50153(9)	335(50)
50288.2(9)	196(149)
50798(3)	271(33)
51081(3)	160(110)
51241(4)	391(37)
51378(2)	263(182)
52195(2)	362(139)
52368(2)	366(208)
52952.3(3)	135(104)
53119(5)	490(49)
53329(6)	118(23)

TABLE V. *(Continued.)*

Energy (eV)	Kernel (meV)
53709(5)	265(30)
53901(6)	218(36)
54315.3(3)	122(94)
54490(5)	267(36)
54694(4)	299(51)
55153.5(3)	162(122)
55660(5)	241(70)
55909.2(10)	185(139)
56617(5)	181(28)
56827(6)	160(24)
57090.1(9)	233(162)
57708(4)	311(34)
58133.7(3)	113(83)
58664(4)	410(50)
58814(2)	274(183)
58993.0(6)	226(191)
59256(8)	530(57)
59509.2(4)	130(92)
60073(5)	399(38)
61143(9)	667(76)
61346(6)	218(44)
61706(6)	420(47)
61951(2)	138(101)
62265.9(2)	74(52)
62499.0(10)	330(243)
63265.9(3)	81(59)
63638(7)	614(63)
64128.4(7)	172(124)
64257(4)	274(159)
64722.1(5)	251(177)
65104.3(4)	269(195)
65418.5(2)	70(59)
65650.3(3)	68(59)
65837.5(6)	76(64)
66151(8)	413(56)
66359.0(3)	103(83)
66503.2(3)	57(48)
67177.3(6)	80(58)
67257(10)	119(45)
67410.4(5)	155(108)
67623.2(4)	255(184)
67884.7(3)	73(62)
68186(7)	406(68)
68275.3(2)	84(71)
68526(7)	258(161)
68588.2(3)	87(72)
69058.3(5)	175(135)
69413.1(3)	248(176)
69943.3(3)	139(116)
70068.7(3)	83(61)

APPENDIX B: NEUTRON WIDTHS OF RESONANCES ASSIGNED AS *s* WAVE

See Table VI for a list of energies and partial width extracted using SAMMY for likely 78Se capture resonances identified as likely s-wave.

TABLE VI. Energies and neutron and gamma partial widths obtained from SAMMY fits for likely *s*-wave resonances of spin $J = \frac{1}{2}$. Only fitting uncertainties are provided.

Energy (eV)	Γ_n (meV)	Γ_γ (meV)
381.862(4)	347(1)	146.1(6)
3198.7(2)	12700(225)	207(3)
5635.2(1)	3930(203)	162(4)
6123(1)	63800(2740)	216(7)
6791.8(2)	7280(361)	191(5)
9217(2)	33300(3960)	142(19)
10908(3)	97200(7120)	288(20)
12360.0(4)	6410(708)	226(8)
18672(3)	62800(6310)	245(18)
19978(3)	31100(4740)	158(11)
21901(2)	36200(5800)	232(17)
23577(1)	7660(2690)	223(19)
24054(2)	16000(3250)	217(14)
25958(2)	14800(3300)	233(15)
29159(7)	40100(16600)	141(23)
29288(3)	15300(7220)	223(27)

[1] C. M. Raiteri, R. Gallino, M. Busso, D. Neuberger, and F. Käppeler, Astrophys. J. **419**, 207 (1993).

[2] N. Nishimura, R. Hirschi, T. Rauscher, A. St. J. Murphy, and C. Cescutti, Mon. Not. R. Astron. Soc. **469**, 1752 (2017).

[3] N. V. Sosnin *et al.* (n_TOF Collaboration), Phys. Rev. C **107**, 065805 (2023).

[4] The Karlsruhe Astrophysical Database of Nucleosynthesis in Stars, online at https://www.kadonis.org/, latest release Kadonis-0.3; I. Dillmann, M. Heil, F. Käppeler, R. Plag, T. Rauscher, and F. K. Thielemann, AIP Conf. Proc. **819**, 123 (2006).

[5] D. A. Brown, M. B. Chadwick, R. Capote, A. C. Kahler, A. Trkov, M. W. Herman, A. A. Sonzogni, Y. Danon, A. D. Carlson, M. Dunn, D. L. Smith, G. M. Hale, G. Arbanas, R. Arcilla, C.R. Bates, B. Beck, B. Becker, F. Brown, R. J. Casperson, J. Conlin *et al.*, Nucl. Data Sheets **148**, 1 (2018).

[6] S. F. Mughabghab, M. Divadeenam, and N. E. Holden, *Neutron Cross Sections* (Elsevier, Amsterdam, 1981), Vol. 1, pp. 34–37.

[7] R. E. Coté, L. M. Bollinger, and G. E. Thomas, Phys. Rev. **136**, B703 (1964).

[8] Kh. Maletski, L. B. Pikel'ner, I. M. Salamatin, and E. I. Sharapov, Sov. J. Nucl. Phys. **9**, 1119 (1969).

[9] J. Julien, R. Alves, S. de Barros, V. D. Nuynh, J. Morgenstern, and C. Samour, Nucl. Phys. A **132**, 129 (1969).

[10] N. Otuka, E. Dupont, V. Semkova, B. Pritychenko, A.I. Blokhin, M. Aikawa, S. Babykina, M. Bossant, G. Chen, S. Dunaeva, R. A. Forrest, T. Fukahori, N. Furutachi, S. Ganesan, Z. Ge, O. O. Gritzay, M. Herman, S. Hlavač, K. Katō, B. Lalremruata *et al.*, Nucl. Data Sheets **120**, 272 (2014).

[11] S. Kamada, M. Igashira, T. Katabuchi, and M. Mizumoto, J. Nucl. Sci. Technol. **61**, 161 (2024).

[12] G. Rugel, I. Dillmann, T. Faestermann, M. Heil, F. Käppeler, K. Knie, G. Korschinek, W. Kutschera, M. Poutivtsev, and A. Wallner, Nucl. Instrum. Methods Phys. Res., Sect. B **259**, 683 (2007).

[13] I. Dillman, M. Heil, F. Käppeler, T. Faestermann, G. Korschinek, K. Knie, M. Poutivtsev, G. Rugel, A. Wallner, and T. Rauscher, PoS Lattice **(PoS NIC-IX)**, 089 (2006).

[14] M. Herman and A. Marcinkowski, Nucl. Phys. A **357**, 1 (1981).

[15] K. Siddappa, M. Sriramachandra Murty, and J. Rama Rao, J. Phys. A: Gen. Phys. **5**, 877 (1972).

[16] C. Guerrero *et al.* (n_TOF Collaboration), Eur. Phys. J. A **49**, 27 (2013).

[17] P. F. Mastinu, R. Baccomi, E. Berthoumieux, D. Cano-Ott, F. Gramegna, C. Guerrero, C. Massimi, P. M. Milazzo, F. Mingrone, J. Praena, G. Prete, and A. R. García, New C_6D_6 detectors: Reduced Neutron Sensitivity and Improved Safety, CERN Technical Report No. n_TOF-PUB-2013-002, 2013 (unpublished).

[18] P. Žugec *et al.* (n_TOF Collaboration), Nucl. Instrum. Methods Phys. Res., Sect. A **812**, 134 (2016).

[19] U. Abbondanno *et al.* (n_TOF Collaboration), Nucl. Instrum. Methods Phys. Res., Sect. A **521**, 454 (2004).

[20] M. C. Moxon and E. R. Rae, Nucl. Instrum. Methods **24**, 445 (1963).

[21] R. L. Macklin and J. H. Gibbons, Phys. Rev. **159**, 1007 (1967).

[22] S. Agostinelli *et al.* (GEANT4 Collaboration), Nucl. Instrum. Methods Phys. Res., Sect. A **506**, 250 (2003).

[23] F. Bečvář, Nucl. Instrum. Methods Phys. Res., Sect. A **417**, 434 (1998), Erratum in Ref. [49].

[24] M. Krtička and S. Valenta, https://www-nds.iaea.org/dicebox/, 2018.

[25] A. J. M. Plompen, O. Cabellos, C. De Saint Jean, M. Fleming, A. Algora, M. Angelone, P. Archier, E. Bauge, O. Bersillon, A. Blokhin, F. Cantargi, A. Chebboubi, C. Diez, H. Duarte, E. Dupont, J. Dyrda, B. Erasmus, L. Fiorito, U. Fischer, D. Flammini *et al.*, Eur. Phys. J. A **56**, 181 (2020).
[26] A. J. Koning, D. Rochman, J.-Ch. Sublet, N. Dzysiuk, M. Fleming, and S. van der Marck, Nucl. Data Sheets **155**, 1 (2019).
[27] M. Barbagallo *et al.* (n_TOF Collaboration), Eur. Phys. J. A **49**, 156 (2013).
[28] R. L. Macklin, J. Halperin, and R. R. Winters, Nucl. Instrum. Methods A **164**, 213 (1979).
[29] N. M. Larson, Updated Users Guide for SAMMY: Multilevel R-matrix Fits to Neutron Data Using Bayes' Equations, Technical Report No. ORNL/TM-9179/R8 (Oak-Ridge National Laboratory, Oak Ridge, TN, 2008).
[30] S. F. Mughabghab, *Atlas of Neutron Resonances*, 6th ed. (Elsevier, Amsterdam, 2018), pp. 34–35.
[31] A. R. Farhan and B. Singh, Nucl. Data Sheets **110**, 1917 (2009).
[32] B. Singh, Nucl. Data Sheets **135**, 193 (2016).
[33] S. Kamada (private communication).
[34] O. Iwamoto, N. Iwamoto, S. Kunieda, F. Minato, S. Nakayama, Y. Abe, K. Tsubakihara, S. Okumura, C. Ishizuka, T. Yoshida, S. Chiba, N. Otuka, J.-C. Sublet, H. Iwamoto, K. Yamamoto, Y. Nagaya, K. Tada, C. Konno, N. Matsuda, K. Yokoyama *et al.*, J. Nucl. Sci. Technol. **60**, 1 (2023).
[35] F. Fröhner, B. Goel, and U. Fischer, FITACS, Computer Code, Technical Report No. ANL-83-4 (Argonne National Laboratory, Chicago, 1983).
[36] R. Capote, M. Herman, P. Oblozinsky, P. Young, S. Goriely, T. Belgya, A. Ignatyuk, A. Koning, S. Hilaire, V. Plujko, M. Avrigeanu, O. Bersillon, M. Chadwick, T. Fukahori, Z. Ge, Y. Han, S. Kailas, J. Kopecky, V. Maslov, G. Reffo *et al.*, Nucl. Data Sheets **110**, 3107 (2009).
[37] J. Lerendegui-Marco *et al.* (n_TOF Collaboration), Phys. Rev. C **97**, 024605 (2018).
[38] M. Dietz *et al.* (n_TOF Collaboration), Phys. Rev. C **103**, 045809 (2021).
[39] T. von Egidy and D. Bucurescu, Phys. Rev. C **72**, 044311 (2005).
[40] M. Herman, Brookhaven National Laboratory Report No. BNL-NCS-44945-05-Rev, 2005 (unpublished).
[41] A. J. Koning, TALYS-1.9, http://www.talys.eu, 2021.
[42] C. Ritter, F. Herwig, S. Jones, M. Pignatari, C. Fryer, and R. Hirschi, Mon. Not. R. Astron. Soc. **480**, 538 (2018).
[43] F. Herwig, S. Diehl, C. L. Fryer, R. Hirschi, A. Hungerford, G. Magkotsios, M. Pignatari, G. Rockefeller, F. X. Timmes, P. Young, and M. E. Bennett, PoS Lattice (PoS NIC X) **053** (2009).
[44] B. Singh, J. Chen, and A. R. Farhan, Nucl. Data Sheets **194**, 3 (2024).
[45] N. Prantzos, C. Abia, S. Cristallo, M. Limongi, and A. Chieffi, Mon. Not. R. Astron. Soc. **491**, 1832 (2020).
[46] S. Cristallo, L. Piersanti, O. Straniero, R. Gallino, I. Domínguez, C. Abia, G. Di Rico, M. Quintini, and S. Bisterzo, Astrophys. J. Suppl. Series **197**, 17 (2011).
[47] D. Vescovi, S. Cristallo, M. Busso, and N. Liu, Astrophys. J. Lett. **897**, L25 (2020).
[48] D. Vescovi, S. Cristallo, S. Palmerini, C. Abia, and M. Busso, Astron. Astrophys. **652**, A100 (2021).
[49] F. Bečvář, Nucl. Instrum. Methods Phys. Res., Sect. A **935**, 240 (2019).